



HAL
open science

Numerical identification method for the non-linear viscoelastic compressible behavior of soft tissue using uniaxial tensile tests and image registration – Application to rat lung parenchyma

A. Bel-Brunon, S. Kehl, C. Martin, S. Uhlig, W.A. Wall

► **To cite this version:**

A. Bel-Brunon, S. Kehl, C. Martin, S. Uhlig, W.A. Wall. Numerical identification method for the non-linear viscoelastic compressible behavior of soft tissue using uniaxial tensile tests and image registration – Application to rat lung parenchyma. *Journal of the mechanical behavior of biomedical materials*, 2014, 29, pp.360-374. 10.1016/j.jmbbm.2013.09.018 . hal-01866351

HAL Id: hal-01866351

<https://hal.science/hal-01866351>

Submitted on 3 Sep 2018

HAL is a multi-disciplinary open access archive for the deposit and dissemination of scientific research documents, whether they are published or not. The documents may come from teaching and research institutions in France or abroad, or from public or private research centers.

L'archive ouverte pluridisciplinaire **HAL**, est destinée au dépôt et à la diffusion de documents scientifiques de niveau recherche, publiés ou non, émanant des établissements d'enseignement et de recherche français ou étrangers, des laboratoires publics ou privés.

1 Numerical identification method for the non-linear
2 viscoelastic compressible behaviour of soft tissue using
3 uniaxial tensile tests and image registration -
4 Application to rat lung parenchyma

5 A. Bel-Brunon^a, S. Kehl^a, C. Martin^b, S. Uhlig^b, W. A. Wall^{a,*}

6 ^a*Institute for Computational Mechanics, Technische Universität München,
7 Boltzmannstrasse 15, 85747 Garching, Germany*

8 ^b*Institute of Pharmacology and Toxicology, Medical Faculty, RWTH Aachen University,
9 Aachen, Germany*

10 **Abstract**

11 This paper presents an improved identification method of the constitutive
12 properties of lung parenchyma. The aim of this work is to determine the non-
13 linear viscoelastic behavior of lung parenchyma with a particular focus on the
14 compressible properties. Tensile tests are performed on living precision-cut
15 rat lung slices. Image registration is used to compute **the displacement field**
16 at the surface of the sample. This allows to identify the compressibility of
17 the tissue. The constitutive model consists of a hyperelastic potential split
18 into volumetric and isochoric contributions and a viscous contribution. This
19 allows the description of the experimentally observed hysteresis loop. The
20 identification is performed numerically: each test is simulated using the real
21 geometry of the sample; the error in the displacement (i.e. the difference
22 between the measured and computed displacements) is minimized with an
23 improved Levenberg-Marquardt algorithm. This global method allows the
24 comparison between several hyperelastic potentials and we can determine

*Corresponding author. Institute for Computational Mechanics, Technische Universität München, Boltzmannstrasse 2, 85747 Garching, Germany. Tel.: +49 089 289 15300. Fax: +49 089 289 15301. E-mail address: wall@lmm.mw.tum.de

25 the most suitable law for rat lung parenchyma. We find that both an ex-
26 ponential potential or a polynomial potential with a first order term and a
27 third or higher order term give similarly satisfactory results. The identified
28 parameters are: for the volumetric contribution: $\kappa = 7.25e4 \pm 2.74e4$ Pa, for
29 the exponential potential: $k_1 = 4.70e3 \pm 1.60e3$ Pa, $k_2 = 5.90 \pm 1.51$, for
30 the polynomial form: $C_1 = 2.87e3 \pm 9.05e2$ Pa, $C_3 = 3.83e4 \pm 1.63e4$ Pa.
31 The identification of the time parameter for the viscous contribution shows
32 that it depends on the loading frequency (0.2 Hz: $\tau = 0.257 \pm 0.042$ s, 0.4
33 Hz: $\tau = 0.123 \pm 0.039$ s, 0.8 Hz: $\tau = 0.050 \pm 0.025$ s). Adding a viscous
34 contribution significantly increases the accuracy of the identification.
35 *Keywords:* lung parenchyma, non-linear viscoelasticity, numerical
36 identification, image registration, uniaxial tensile test, compressibility

37 1. Introduction

38 Characterizing the mechanical behavior of lung tissues has been the sub-
39 ject of several scientific studies as it is required to model the global and
40 local behavior of the lung. A computational model of the whole lung could
41 help understanding several phenomena related to lung diseases. For instance,
42 acute respiratory distress syndrome (ARDS) is a disease that alters the me-
43 chanical behavior of the lung parenchyma (Kallet and Katz, 2003). When a
44 patient suffering from ARDS is mechanically ventilated to help him breathe,
45 healthy and diseased areas are deformed but the compliance difference of
46 these two tissues can lead to a local overstretching in the parenchyma. A
47 lung model including mechanical properties of both healthy and diseased
48 parenchyma could help locating and quantifying the possible overstretching

49 occurring within the parenchyma and adapting the curing protocol to avoid
50 it. A comprehensive model of the lung is currently developed in our group
51 including among others, structure and fluid phenomena (Wall et al., 2010).

52 Lung parenchyma consists of alveolar tissue, including respiratory bron-
53 chioles, alveolar ducts and terminal bronchioles. At the macroscale (a few
54 cm), it can be considered as homogeneous but at the microscale (alveolar
55 scale, *i.e.* a mm), it exhibits a foam-like structure due to the alveoli, which
56 are inflated with air during breathing. Therefore, unlike most of the soft
57 tissues commonly studied (e.g. abdominal organs, skin, aorta), it cannot be
58 considered as incompressible at the macroscale as its main function is to be
59 inflated. Most of the previous studies to characterize the lung parenchyma
60 have investigated its non-linear elasticity and viscoelasticity but the com-
61 pressible properties have not been characterized sufficiently so far.

62 To characterize lung parenchyma, the few available previous studies de-
63 scribe mostly uniaxial tensile tests on tissue slices. Briefly, in terms of elas-
64 ticity, either an exponential potential (Navajas et al., 1995) or a polynomial
65 potential (Rausch et al., 2011) describe rather accurately the uniaxial behav-
66 ior of the lung parenchyma. Gao et al. performed biaxial tensile tests and
67 concluded that an exponential law was the best fit for the tissue behavior
68 (Gao et al., 2006). A volumetric component of the constitutive law is only
69 assessed in (Rausch et al., 2011); however the method to identify the vol-
70 umetric parameters of the constitutive law only relied on the displacement
71 of a single location in the sample and the measurement of this displacement
72 was done by hand.

73 In terms of viscoelasticity, uniaxial tensile tests were used to characterize

74 the dynamic response of the tissue. Different frameworks helped quantify-
75 ing the tissue viscosity, the most common (Mijailovich et al., 1994; Navajas
76 et al., 1995; Romero et al., 2011; Pinart et al., 2011; Yuan et al., 1997) being
77 quasilinear viscoelasticity proposed by Fung that decouples the elastic and
78 viscous phenomena and allows accounting for elastic non-linearities (Fung,
79 1993). In these studies, harmonic distortion, loss and storage moduli as well
80 as elastance, resistance and hysteresivity of the tissue were computed with
81 the help of a Fourier transform. These parameters allow the investigation
82 of the influence of loading factors - like stress amplitude, strain amplitude,
83 frequency - or pathologies - like fibrosis (Dolhnikoff et al., 1999), acute lung
84 injury (Ingenito et al., 1994; Rocco et al., 2001) - on the material parame-
85 ters. A review of the elastic and viscous characterization of lung tissue, in
86 particular using tests on excised samples, is given in (Suki and Bates, 2011).
87 Another framework is proposed by (Holzapfel and Gasser, 2001) to account
88 for the three-dimensional non-linear viscoelasticity of fiber-reinforced com-
89 posites: the hyperelastic potential associated with the elastic behavior of the
90 tissue is modified by a viscous contribution. This framework is particularly
91 suited for a direct use in nonlinear continuum mechanics based simulations,
92 this is why this approach is chosen in the present paper.

93 The aim of this paper is to determine a non-linear viscoelastic constitu-
94 tive employing novel experimental and identification methods. The paper is
95 divided into five parts: the first part covers the description of the experimen-
96 tal methods, particularly the optical method to measure the displacement
97 field on the sample. In the second part, the numerical model and the consti-
98 tutive law proposed for the lung parenchyma are detailed. The third, fourth

99 and fifth parts are focused on the identification method, the results and the
100 discussion, respectively.

101 **2. Uniaxial tensile tests on living PCLS**

102 Since the preparation of the samples and the experimental set-up are
103 described in a previous paper (Rausch et al., 2011), only the main features
104 are recalled here.

105 *2.1. Preparation of the samples*

106 The Precision-Cut Lung Slices (PCLS) are prepared from three isolated
107 rat lungs as previously described in (Martin et al., 1996). The lungs are
108 dissected from the animal, filled with an agarose solution (1.5%) via the
109 trachea and put on ice to allow the agarose to cool down and solidify. The
110 lung lobes are separated and cut into tissue cylinders using a coring tool.
111 The obtained cylinders have a diameter of 14 mm; they are then cut into
112 slices using a Krumdieck tissue slicer (Alabama Research and Development,
113 Munford, AL). The thickness is set to 400 μm . The two sides of the round
114 slices are trimmed with two parallel razor blades giving the tissue strip a
115 width of 7.0 mm. The strips are incubated in minimal essential medium
116 (MEM) and the agarose is washed out by frequently changing the medium
117 within the first 4 hours and completing an overnight incubation. As shown
118 in (Martin et al., 1996), the obtained PCLS are viable for three days. In
119 this protocol, the rat samples are tested within 48 hours after death, which
120 guarantees that the tissue is still living while being tested (Martin et al.,
121 1996) ; preliminary studies showed that the mechanical properties are not
122 changing within 3 days (data not shown). The samples are kept in saline

123 solution in the fridge (4°C) until they are tested. Tab. 1 sums up the
 124 specimen numbers.

Name	Number of samples per frequency		
	0.2 Hz	0.4 Hz	0.8 Hz
G	7	5	4
I	4	4	4
J	3	3	4

Table 1: Samples description.

125 2.2. Experimental set up

126 The samples are tested using a Bose ElectroForce 3100 uniaxial device
 127 (Bose Cooperation, Eden Prairie, USA). The samples are fixed onto the ma-
 128 chine using specifically designed clamps to prevent sliding and damage (Fig.
 129 1). The moving clamp displacement is recorded using the internal displace-
 130 ment sensor of the tensile machine (range of ± 2.5 mm with a resolution of
 131 $12.5 \mu\text{m}$); the other clamp is connected to the machine through a force sensor
 132 (range of ± 0.5 N with a resolution of 2.5 mN). Finally, a digital microscope
 133 is placed perpendicular to the sample plane to record the test. The images
 134 provided by the microscope are $640 \times 480 \text{ px}^2$.

135 Images of each test are recorded to perform image registration. Such
 136 an optical method allows the computation of the displacement field at the
 137 surface of the sample. It consists in mapping images of the sample in its
 138 undeformed and deformed state. This mapping is based on the gray-level
 139 distribution of the image; it requires for the images a good resolution and
 140 a stable gray-level distribution which has to exhibit a random pattern. If

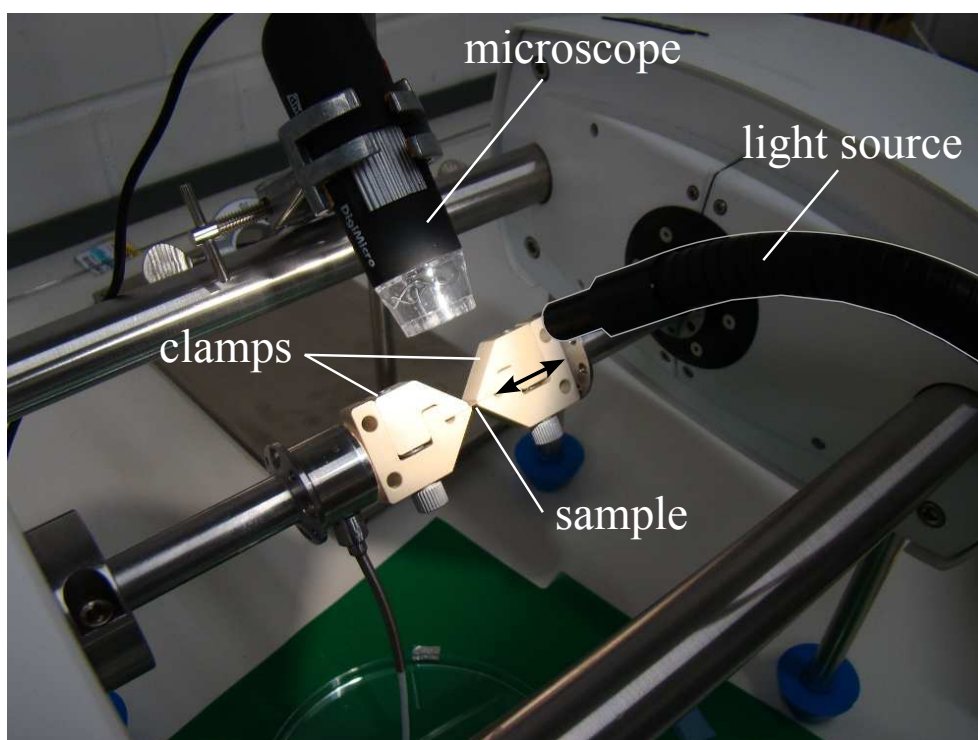


Figure 1: Experimental setup. The double arrow shows the tensile direction.

141 the gray-levels are affected by a modification of the lightening or by light
142 reflections at the surface of the sample, artifacts will occur in the computation
143 of the displacement field.

144 In our case, the registration procedure relies on the microstructure of
145 the lung parenchyma. By using a lightening that goes partially through the
146 sample, this microstructure can be visualized; hence, the application of an
147 additional random pattern using paint - as it is usually necessary when using
148 an optical method to compute the experimental displacement - is superfluous.
149 However, due to the low density of the tissue, the light rays intensity is hardly
150 lessened when going through the tissue. Putting the light source and the
151 microscope directly opposite to each other on both sides of the sample leads to
152 a general overexposure, as well as a modification in the overall light intensity
153 in the image during the sample stretching (since the sample gets thinner while
154 being stretched, the penetration of light gets stronger). The solution to have
155 a good insight of the microstructure and a satisfactory light intensity for the
156 images was to put the light source on one side and slightly above the sample
157 (Fig. 1); therefore the light is slightly scattered which reduces reflecting
158 signals. The drawback of this method is that it does not completely prevent
159 the occurrence of shining points, where the light is reflected on the wet surface
160 of the sample. Even if not numerous, these parasite pixels can create artifacts
161 during the registration procedure. However, the image registration algorithm
162 helps smoothing these possible artifacts.

163 *2.3. Testing protocol*

164 *2.3.1. Thickness measurement and placement on the machine*

165 The first step of the experimental protocol is to measure the actual thick-
166 ness of the sample. Although the cutting tool is very accurate, the softness
167 of the lung tissue and its compressibility inevitably lead to a variability in
168 the thickness. To accurately measure the global sample thickness, a light
169 microscope and a micrometer are used as shown in Fig. 2. Two microscopic
170 slides are placed on each other and under the microscope; a pattern is drawn
171 on the upper one. The microscope is focused on the pattern and the vertical
172 position of the microscope plate is measured by a micrometer. The sample is
173 then placed between the two microscopic slides and the water is wiped up so
174 as not to create a water film between the two microscopic slides. At this stage
175 the upper slide is in a higher position due to the thickness of the sample and
176 the microscope does not focus on the pattern anymore. Then, the focus is
177 adjusted on the upper slide pattern again; the resulting displacement of the
178 microscope plate is the thickness of the sample, measured by the micrometer.
179 The thickness is measured within an accuracy of 10 μm .

180 Once the thickness has been measured, the sample is hydrated again
181 with saline solution. It is placed on a piece of aluminum foil. The foil and
182 sample are placed in the clamps which are slightly fastened until the sample
183 is sufficiently fixed to be able to remove the aluminum. The two clamps are
184 then more firmly fastened to prevent sliding but also possible damage of the
185 tissue. Finally, the extra water content is mopped up with paper so as to
186 avoid measuring artificial forces due to surface tension effects of the water
187 layer.

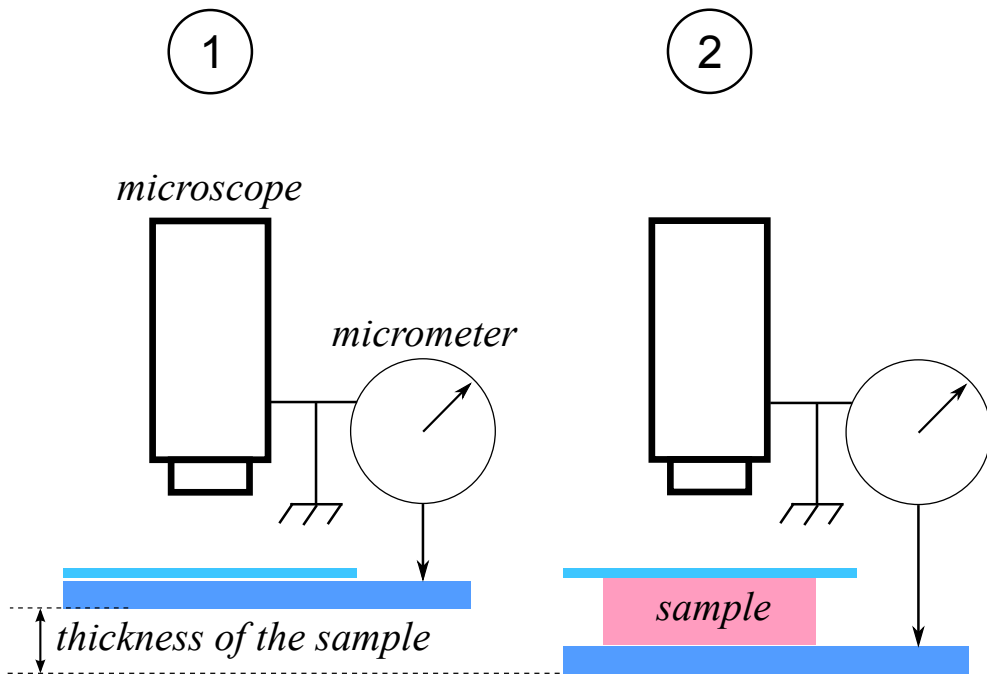


Figure 2: Method to measure the thickness of the sample: first, we focus the microscope on the upper slide without sample. Second, once the sample is put between the two slides, the microscope is focused again on the upper slide and the displacement of the microscope plate is measured by a micrometer. The measured displacement is the thickness of the sample.

188 The initial length of the sample, i.e. the initial distance between the
189 clamps, is set to 2.0 mm.

190 *2.3.2. Preconditioning and tensile test*

191 In this work, the aim is to investigate the tissue behavior in the range
192 of large strains. Preliminary tensile tests conducted on lung samples showed
193 that when stretched to 50% strain and released, the sample exhibits a residual
194 strain. Besides, during cycling tensile loading, the viscoelastic nature of
195 the tissue leads to a transitory phase where the force-displacement cycles
196 cannot be superimposed. One can assume that during breathing, the tissue
197 exhibits a rather repeatable behavior from one cycle to the other. Therefore,
198 a preconditioning phase is applied to the tissue to first, stabilize its residual
199 strain and second, to stabilize the hysteresis loop obtained while cycling the
200 sample.

201 In the present case, the preconditioning includes two main steps: first,
202 the sample is stretched from 0 to 0.2 mm at a constant velocity of 0.5 mm/s
203 and maintained 10 s at 0.2 mm; then this phase is repeated for 0.4, 0.6 and
204 0.8 mm. The tissue is then released to a stretch of 0.2 mm for 30 s. Second,
205 the tissue is cycled between 0.2 and 1.2 mm for 10 cycles. The nine first
206 cycles are used for preconditioning while the tenth is the actual tensile test.
207 We found that nine cycles were enough to stabilize the cycle (see Sec.5.1).

208 *2.3.3. Reference state*

209 The preconditioning is performed to stabilize the residual strain; it leads
210 to the definition of the stress-free reference state which is different from the
211 initial state. We choose to perform the tensile test in a range that makes

212 the sample slightly buckle at the minimum stretch. Therefore, when cycling,
213 the force is slightly negative (compressive force) and becomes positive. The
214 state corresponding to a force equal to zero is defined as the reference state
215 for the image registration procedure. In practice, the zero-force state does
216 not necessarily match one of the registration images for sampling frequency
217 reasons; in that case, we choose the image that corresponds to the smallest
218 force to define the reference geometry of the sample. Over all the samples,
219 the initial force is always below 5% of the maximal force of the test. We
220 also assume that the difference between reference and initial configurations
221 is small enough to consider that the initial thickness is still applicable to the
222 reference configuration. Indeed, the reference state corresponds experimen-
223 tally to a clamp displacement of around 0.1 mm.

224 *2.4. Postprocessing by image registration*

225 Using a full-field measurement method when testing soft material has
226 several advantages. First, cutting samples of soft tissues of accurate dimen-
227 sions is a difficult task; even with precision-slicing apparatus and procedure
228 as described in Section 2.1, one cannot always obtain perfectly rectangular
229 samples. Then, such thin samples are difficult to handle and to place in the
230 clamps. The method described previously eases this procedure but we can
231 for instance not perfectly control the orientation of the sample with respect
232 to the loading direction. Finally, screwing the clamps to properly prevent
233 sliding without damaging the sample requires some care; it can happen that
234 the sample is not squeezed enough and experiences sliding during the test.
235 For these reasons, it makes sense to use optical measurements additional to
236 the force and global displacement information to know more accurately the

237 actual displacement of the sample during the experiment.

238 Besides, the present work is focused on a compressible tissue. The identi-
239 fication procedure therefore requires information about the evolution of the
240 width of the sample, which is directly related to the compressibility of the tis-
241 sue. Global longitudinal measurement would not be sufficient to accurately
242 identify the compressibility material constant.

243 As mentioned before, image registration consists in mapping two images
244 of the sample that represent two different deformation states. These two
245 images are called source image and target image; they both contain a scalar
246 field that is a gray-level distribution over the pixels of the image. Image
247 registration consists in finding the displacement field that minimizes the gap
248 between the target image and the source image once it is deformed by this
249 displacement field. We describe here the main features of this minimization
250 procedure; more detailed information can be found in the cited papers.

251 The source and target images are denoted by $I_s(\mathbf{X})$ and $I_t(\mathbf{x})$ respectively
252 where \mathbf{x} and \mathbf{X} are the spatial and material coordinates respectively.

253 For a so-called *forward* transformation, registering the two images consists
254 in minimizing the error \mathcal{D} with respect to the transformation φ (Haber et al.,
255 2009):

$$\mathcal{D}[\varphi(\mathbf{X})] = \int_{\Omega_x} [I_s(\varphi^{-1}(\mathbf{x})) - I_t(\mathbf{x})]^2 dx \quad (1)$$

256 where $\varphi : I_s \mapsto I_t$ (Fig. 3) so that $\mathbf{x} = \varphi(\mathbf{X}) = \mathbf{X} + \mathbf{u}$ with \mathbf{u} a spatially
257 varying displacement field. The solution \mathbf{u}^* of the minimization is written:

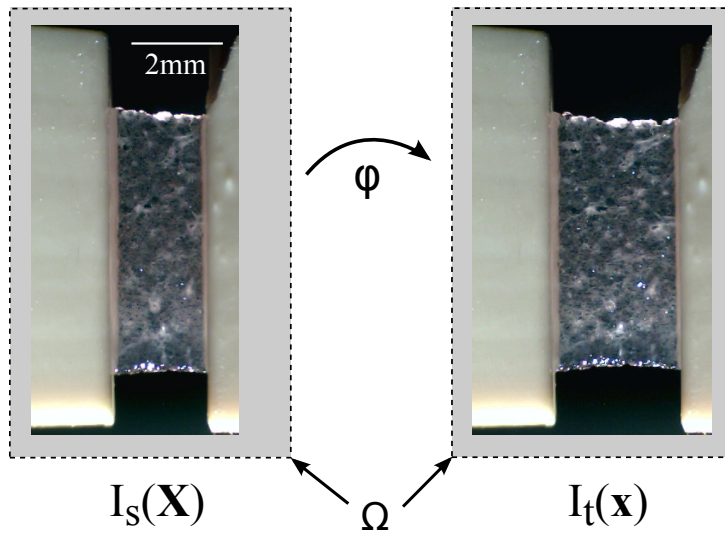


Figure 3: Source image (left) and target image (right).

$$\mathbf{u}^* = \arg \min_{\mathbf{u} \in L^2} \mathcal{D} \quad (2)$$

258 An elastic regularization \mathcal{R} is added to ensure the well-posedness of the
 259 optimization problem (Modersitzki, 2004; Fischer and Modersitzki, 2008).

260 The minimization is therefore:

$$\mathbf{u}^* = \arg \min_{\mathbf{u} \in L^2} [\mathcal{D} [I_s, I_t] + \alpha \mathcal{R}(\mathbf{u})] \quad (3)$$

261 where the weighting factor α is set to 0.1 in this work.

262 We minimize \mathcal{D} using a Gauss-Newton optimization scheme (Haber and
 263 Modersitzki, 2006) as well as a multiresolution approach (Lester and Arridge,
 264 1999) (Fig. 4). First, from the pixel-size grid, i.e. the image recorded during
 265 the experiment, several coarser and coarser grids are successively created by
 266 filtering and sampling the gray-level field of the image at the one-level finer

267 scale. We obtain n levels of resolution. The minimization starts at the coarser
 268 level n ; the result \mathbf{u}_n of the minimization of \mathcal{D} is linearly interpolated over
 269 the grid at level $n - 1$; \mathbf{u}_n^{n-1} is used as the initial guess for the minimization
 270 at level $n - 1$. This procedure is repeated until $\mathbf{u}_1 = \mathbf{u}^*$ - at the pixel level -
 271 is determined.

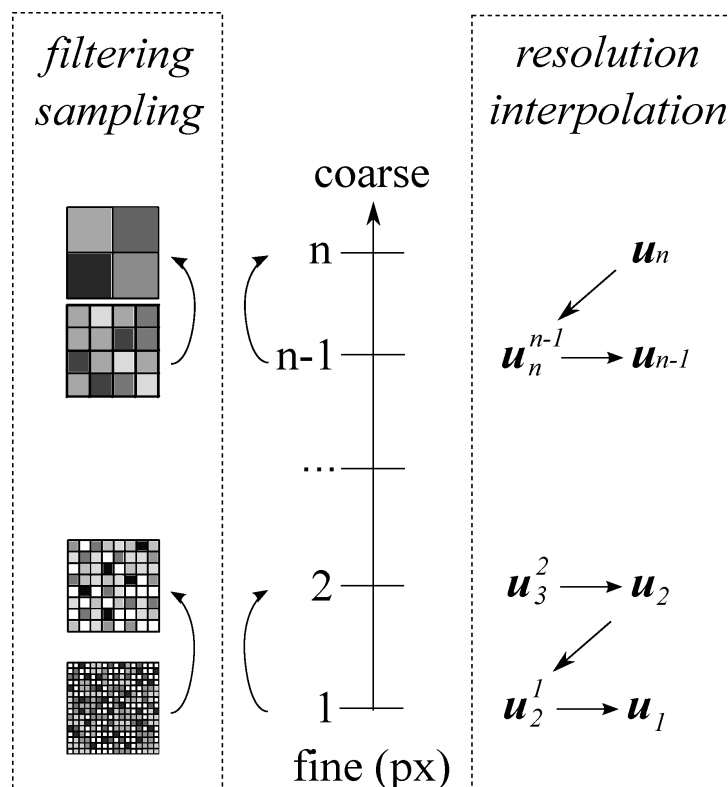


Figure 4: Multiresolution approach to solve the minimization problem of the image registration. \mathbf{u}_i is the solution of the minimization at level i . \mathbf{u}_i^j is the linear interpolation of \mathbf{u}_i over level j and is the initial guess for the resolution at level j . $\mathbf{u}_1 = \mathbf{u}^*$ is the solution of the problem. The finer grid (lower left) is the image recorded during the test.

272 In our case, five levels of resolution are used. The image registration
 273 algorithm is implemented in Matlab, as well as the post-processing of the

274 registration results (creation of the input file for the simulation).

275 The overall registration procedure can be computed in two different ways:
276 sequentially or incrementally. The sequential method consist in defining a
277 reference image (corresponding to the reference state of the sample) and
278 register all the other images (while the sample is stretched) with respect
279 to this reference image. The incremental method consists in updating the
280 reference image: image $n + 1$ is registered with respect to image n . In this
281 case, the Finite Element mesh (see next section) needs to be updated at each
282 new reference image: the position of the nodes of the FE-mesh at step n is
283 updated using the result of the registration between images $n - 1$ and n . Sec.
284 5.2 gives a comparison of the two methods.

285 The images provided by the microscope are 640×480 px², corresponding
286 to 15.2×11.4 mm². The registration procedure guarantees an accuracy of
287 a pixel size of 0.023 mm.

288 **3. Numerical model of the lung parenchyma samples**

289 *3.1. Finite Element model*

290 The numerical identification procedure is based on the simulation of the
291 experimental test and the minimization of the error between the simulated
292 and the experimental displacements. In order to simulate the test, a zone of
293 interest (ZOI) is defined on the reference image and a Finite Element mesh is
294 created on this ZOI. The shape of the ZOI is quadrangular but not necessarily
295 rectangular. The registration procedure is computed on the entire image but
296 only the results in the ZOI are further used for the identification. The Matlab
297 function *interp2* is used to interpolate the computed displacements on the

298 nodes of the FE-mesh. The thickness that was experimentally measured is
299 defined as the initial thickness of the simulated sample.

300 The simulation is performed using our in-house multi-purpose research
301 software platform *BACI*. The input data for the simulation of the test are
302 the FE-mesh, the material law with the initial guess of parameters and the
303 boundary conditions.

304 *3.2. Constitutive law*

305 The aim of this study is to identify a suitable visco-hyperelastic consti-
306 tutive model for lung parenchyma and determine the corresponding model
307 parameters. The model that we use in the present case is a generalized
308 Maxwell model with different hyperelastic contributions.

309 The hyperelastic contribution is described in details in (Rausch et al.,
310 2011). Briefly, a hyperelastic toolbox is implemented in *BACI* which allows
311 the combination of several different Strain Energy Functions (SEF). We only
312 mention here the isotropic SEF as the lung parenchyma is isotropic. The
313 SEF are of two types: coupled and decoupled. A coupled SEF is based
314 on the overall strain tensor, while a decoupled SEF is split into volumetric
315 and isochoric contributions. The decoupled contributions are all polyconvex
316 and stress-free in the reference state, which allows to sum them up without
317 further condition.

318 In our case, only decoupled potentials are used due to the higher variety
319 of available potentials of this form than for coupled potentials.

320 The viscous contribution is based on the work of (Holzapfel and Gasser,
321 2001). A viscous part is added to the hyperelastic contribution based on a
322 generalized Maxwell model. In this paper, we consider the basic form of the

323 generalized Maxwell model, i.e. a dashpot in parallel with a spring. The
 324 general form of the potential is the following:

$$\psi = \psi^\infty(I_i) + \gamma(\mathbf{C}, \mathbf{\Gamma}) \quad (4)$$

325 where ψ^∞ is the hyperelastic potential and γ is the dissipative potential.
 326 This theoretical framework is detailed for the isotropic case in Appendix A;
 327 details for anisotropic cases can be found in (Holzapfel and Gasser, 2001).

328 Similar to the right Cauchy-Green strain tensor \mathbf{C} being the kinematic
 329 conjugate of the elastic second Piola-Kirchhoff stress tensor \mathbf{S} , $\mathbf{\Gamma}$ is the kine-
 330 matic conjugate of the fictitious stress tensor \mathbf{Q} . These stress tensors are
 331 expressed by:

$$\mathbf{S}^\infty = 2 \frac{\partial \psi^\infty}{\partial \mathbf{C}} \quad (5)$$

$$\mathbf{Q} = -2 \frac{\partial \gamma}{\partial \mathbf{\Gamma}} \quad (6)$$

332 \mathbf{Q} is a non-equilibrium stress; therefore, $\mathbf{Q} = \mathbf{0}$ when $t \rightarrow \infty$. The
 333 evolution of \mathbf{Q} is governed by an equation of evolution:

$$\dot{\mathbf{Q}} + \frac{1}{\tau} \mathbf{Q} = \beta \dot{\mathbf{S}} \quad (7)$$

$$\mathbf{Q}|_{t=0} = \mathbf{0} \quad (8)$$

334 where τ defines a relaxation time and β is a non-dimensional free-energy
 335 factor. The global stress tensor is therefore $\mathbf{S} = \mathbf{S}^\infty + \mathbf{Q}$. The elasticity

336 tensor is also expressed as the sum of an elastic summand and a viscous
337 summand (Eq. 9).

$$\mathbb{C} = \mathbb{C}^\infty + \mathbb{C}^{vis} \quad (9)$$

338 Appendix A and Appendix B sum up the formulas used to compute stress
339 and elasticity tensors for the isotropic case and with the assumption that the
340 viscous effect is the same for isochoric and volumetric contributions, that is
341 to say that a single (τ, β) couple is used.

342 The hyperelastic potentials tested in the present work are summed up in
343 Tab. 2. Only isochoric potentials involving the first invariant are identified
344 as it was shown in (Rausch et al., 2011) that potentials with both the first
345 and the second invariants did not lead to a significant decrease of the error
346 in the identification. We compared several combinations of hyperelastic po-
347 tentials to find out which one gives the best fit. Tab. 3 displays the tested
348 combinations.

349 4. Identification method

350 The identification procedure consists in minimizing the error between
351 computed and experimental displacements for the last cycle, *i.e.* both the
352 loading and unloading curves are taken into account. The input data for this
353 inverse analysis are the simulation data mentioned before and the experimen-
354 tal displacements at the nodes of the FE-mesh that are taken into account
355 for the cost function calculation - typically all the degrees of freedom of the
356 FE-mesh nodes that are not kinematically constrained (Fig. 5).

Vol.	Sussman-Bathe	$\psi_{vsb} = \frac{\kappa}{2}(J - 1)^2$
	Ogden	$\psi_{vo} = \frac{\kappa}{4}(-2 \ln J + J^2 - 1)$
	Penalty	$\psi_{vp} = \epsilon \left(J^\gamma + \frac{1}{J^\gamma} - 2 \right)$
Iso.	Polynomial order n	$\psi_{ipn} = c_n(\bar{I}_1 - 3)^n$
	Exponential	$\psi_{ie} = \frac{k_1}{2k_2} \left[e^{k_2 \left(\frac{\bar{I}_1}{3} - 1 \right)} - 1 \right]$

Table 2: Volumetric and isochoric hyperelastic potentials tested in this work. Parameters in red are to be identified. Sussman-Bathe from (Doll and Schweizerhof, 2000). Ogden from (Ogden, 1974). Penalty from (Balzani et al., 2006). Polynomial from a split and extension of Yeoh’s potential (Yeoh, 1993). Exponential from (Delfino et al., 1997).

A	$\psi = \psi_{vo} + \psi_{ip1} + \psi_{ip2} + \psi_{ip3}$
B	$\psi = \psi_{vo} + \psi_{ip1} + \psi_{ip3}$
C	$\psi = \psi_{vo} + \psi_{ip1} + \psi_{ip2}$
K	$\psi = \psi_{vo} + \psi_{ip1} + \psi_{ip4}$
P	$\psi = \psi_{vo} + \psi_{ie}$

Table 3: Identified hyperelastic potentials.

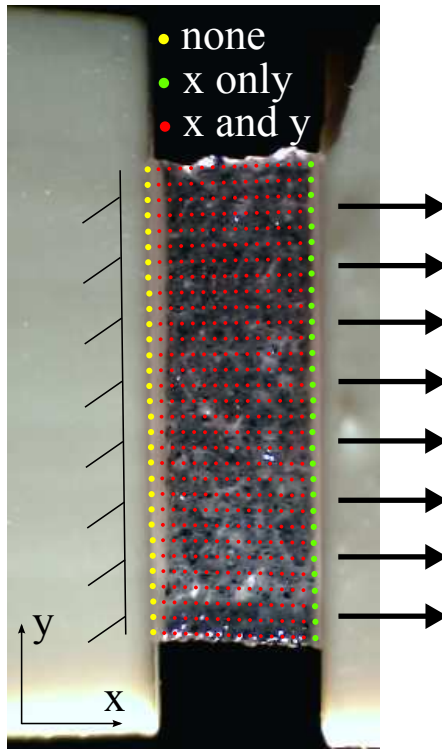


Figure 5: Degrees of freedom used for the inverse analysis. The nodes at the fixed clamp are not used. Only the x-displacement of the moving clamp nodes is used; for the other nodes, the two degrees of freedom are used.

357 The minimization follows a pseudo-transient continuation type scheme.
 358 The constitutive parameters of each summand of the material law and the
 359 associated viscous contribution are stored in the parameter vector \mathbf{p} ; its
 360 size is n_p . For each loop of the inverse analysis, $n_p + 1$ simulations are
 361 performed: n_p simulations with only one modified element of \mathbf{p} ($p(i) = p(i) +$
 362 $a + b \times p(i)$, where a and b are user-defined perturbation parameters) and one
 363 simulation with unperturbed \mathbf{p} . These simulations allow the determination
 364 of the Jacobian matrix \mathbf{J} of the problem (Eq. 10) and the computation of
 365 the new set of parameters $\mathbf{p} = \mathbf{p} + \Delta\mathbf{p}$ (Eq. 11,12)

$$\mathbf{J} = \begin{pmatrix} \frac{\partial \mathbf{u}_1}{\partial p_1} & \dots & \frac{\partial \mathbf{u}_1}{\partial p_{n_p}} \\ \vdots & & \vdots \\ \frac{\partial \mathbf{u}_n}{\partial p_1} & \dots & \frac{\partial \mathbf{u}_n}{\partial p_{n_p}} \end{pmatrix} \quad (10)$$

$$\Delta\mathbf{p} = [\mathbf{J}^T \mathbf{J} + \mu \text{diag}(\mathbf{J}^T \mathbf{J})]^{-1} \mathbf{J}^T \mathbf{R} \quad (11)$$

$$\mathbf{R} = \begin{pmatrix} \mathbf{r}_1 \\ \vdots \\ \mathbf{r}_n \end{pmatrix} = \begin{pmatrix} \mathbf{u}_{1,sim} - \mathbf{u}_{1,exp} \\ \vdots \\ \mathbf{u}_{n,sim} - \mathbf{u}_{n,exp} \end{pmatrix} \quad (12)$$

366 where \mathbf{u}_i is the displacement at node i . The criterion of convergence of
 367 the minimization is based on the gradient of the error $\nabla(e)$ where e is the
 368 cost function, i.e. the sum of the error at all nodes and all time steps.

369 The parameters of the inverse analysis are therefore the convergence cri-
 370 terion, the maximum number of optimization loops, the perturbation param-
 371 eters a and b and an initial regularization factor μ .

372 A nested parallelization implemented in *BACI* allows computing these
373 simulations in parallel, each simulation being itself also computed in parallel;
374 regardless of n_p , one loop of the inverse analysis lasts as long as the longest
375 of the $n_p + 1$ simulations, instead of $n_p + 1$ times the time of one simulation.

376 For each combination of one volumetric potential and possibly several
377 isochoric potentials of Tab. 2, a purely hyperelastic identification is done
378 first, then the viscous contribution is added, which means that an additional
379 parameter τ is to be identified - in this work we set β to 1 and do not identify
380 it. The results of the first identification are used as initial guesses for the
381 viscoelastic identification. During this second phase, both the hyperelastic
382 and the viscous parameters are optimized.

383 5. Results

384 The identification results are statistically analyzed using the non-parametric
385 Mann-Whitney test (Mann and Whitney, 1947); the *p-factor* is indicated
386 when a tendency is significant.

387 5.1. Force versus displacement curves

388 Fig. 6 shows the evolution of the hysteresis loop during the ten cycles
389 of the tensile loading. The hysteresis loop decreases and stabilizes; only the
390 last cycle is taken into account for the identification.

391 5.2. Comparison between sequential and incremental image registration

392 The displacements obtained with the incremental and sequential methods
393 are compared in Fig. 7 and 8. Fig. 7 shows that when the stretch increases
394 (from image 4 to image 14 in that case), the gap between the two methods

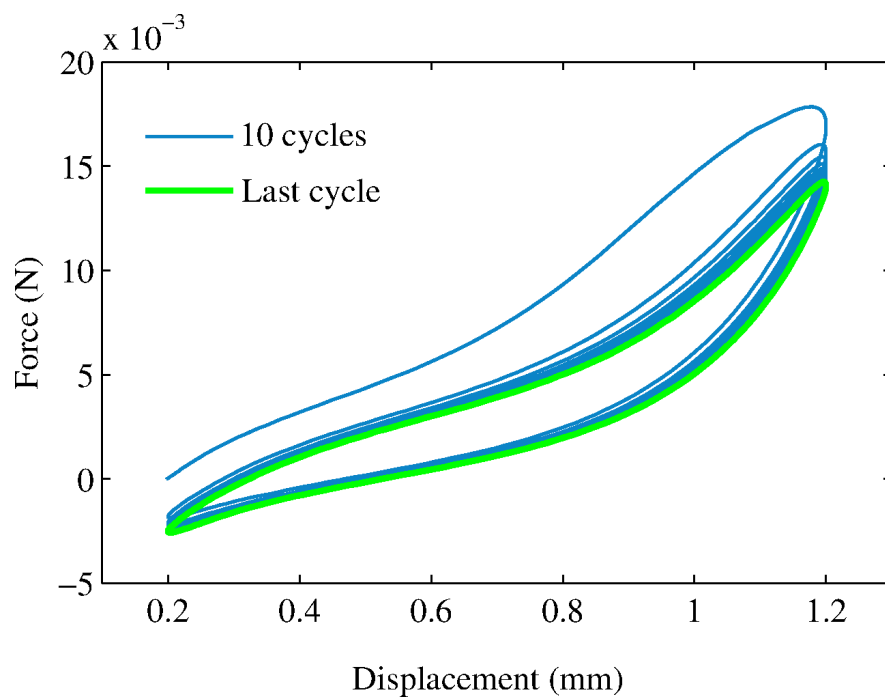


Figure 6: Example of measured curve over ten cycles of tension loading (sample from rat G, frequency: 0.4 Hz). The displacement displayed here is measured by the sensor of the tensile machine.

395 increases but remains small (less than 2% of the maximum displacement
 396 in x-direction). Fig. 8 shows that the incremental method gives a slightly
 397 better result as the new position of the FE-mesh nodes corresponds better
 398 to the visually expected one (the displacement of the moving clamp is
 399 better). That is why we choose the incremental method.

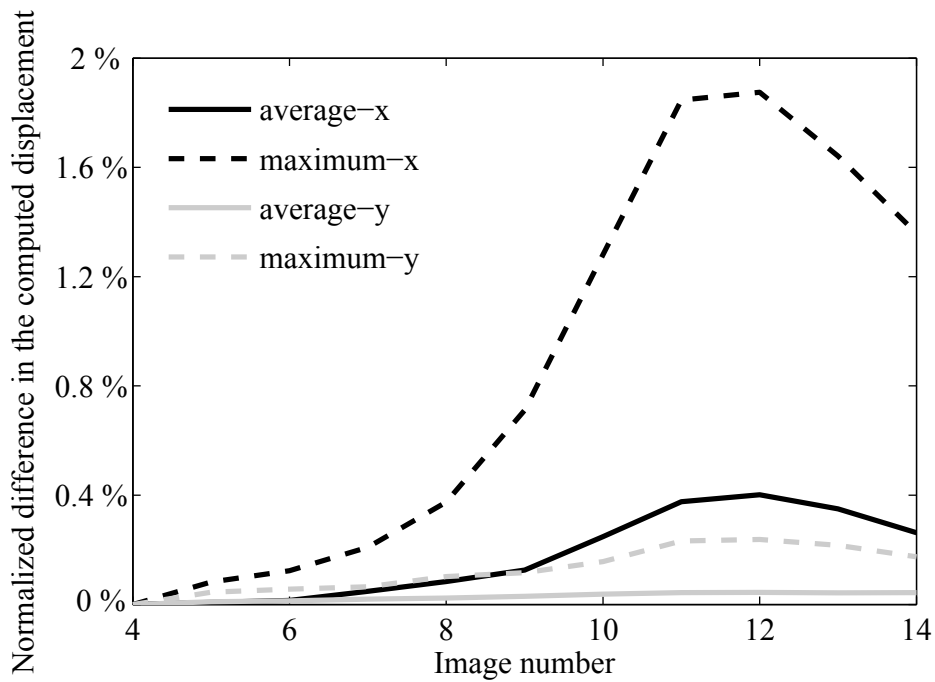


Figure 7: Difference of the displacements computed with the incremental and sequential image registration. At each image, average values and maximum values (over all the FE-mesh nodes) of the gap in the x- and y-directions are normalized by the maximum value of the x- and y-displacements respectively.

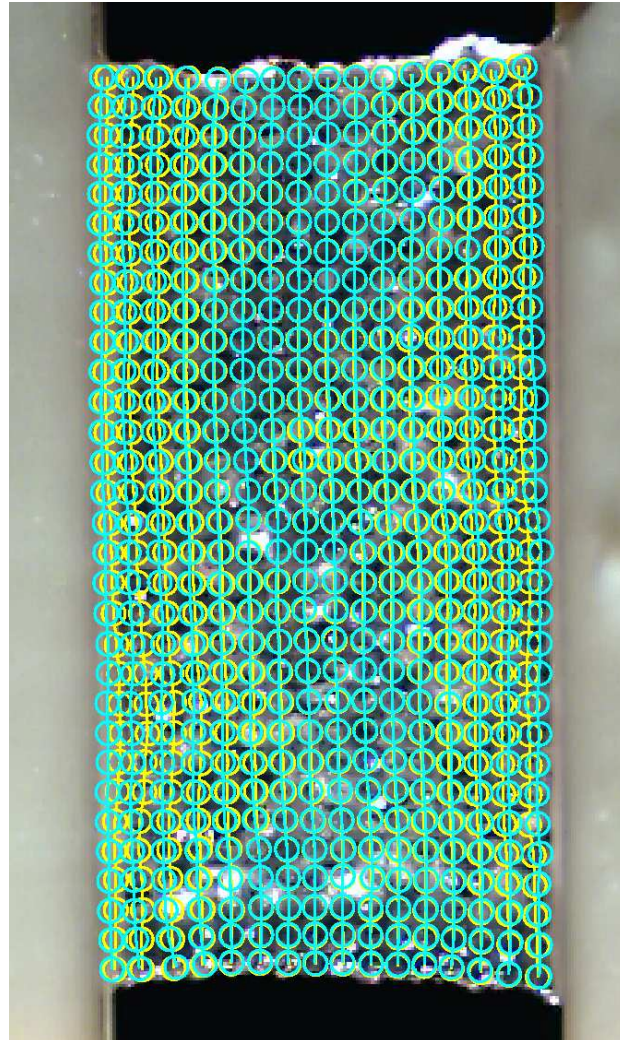


Figure 8: Position of the FE-mesh nodes superimposed on the test picture: position computed by the incremental (blue) and sequential (yellow) image registration methods, for a deformed image. The moving clamp is the right one.

400 *5.3. Convergence of the identification procedure*

401 Parametric studies have been conducted to ensure that the present iden-
402 tification method is robust and valid. In the following, the criterion of con-
403 vergence is $\nabla(e) \leq 10^{-6}$.

404 *Convergence using artificial data.* For this study, artificial data are generated
405 using one of the experiments. A test is simulated with experimental load
406 conditions and an arbitrary set $\hat{\mathbf{p}}$ of material parameters. The computed
407 displacements are used to create a new input file. We then proceed to identify
408 the material parameters of the same law using this file from an arbitrary
409 initial guess, and check that the identified parameters coincide with $\hat{\mathbf{p}}$. This
410 procedure has been conducted using a hyperelastic potential of the following
411 form :

$$\psi = \psi_{vo} + \psi_{ip1} + \psi_{ip3} \quad (13)$$

412 For a total number of elements from 250 to 4410, the maximal value of the
413 average error on the three identified parameters is 0.00731 % (250 elements)
414 which shows convergence to the right values (target values: $\kappa = 30$ kPa, $C_1 =$
415 5 kPa, $C_3 = 10$ kPa; initial guess: $\kappa = 50$ kPa, $C_1 = 0.5$ kPa, $C_3 = 5$ kPa).
416 These values were obtained after 9 to 11 identification loops.

417 To study the convergence of the viscoelastic identification, one viscous
418 constant τ is added. In that case, four parameters are to be identified (target
419 values: $\kappa = 70$ kPa, $C_1 = 3.5$ kPa, $C_3 = 33$ kPa, $\tau = 0.1$; initial guesses: $\kappa =$
420 30 kPa, $C_1 = 5$ kPa, $C_3 = 50$ kPa, $\tau = 0.05$). A single FE-mesh size of 1210
421 elements is used. The identification leads to an error on the target value in

422 the order of 1 % for τ and 0.05 % for the other parameters. The convergence
 423 is therefore very satisfactory.

424 *Influence of the FE-mesh size.* Fig. 9 shows the result of the identification
 425 of the law of Eq. (13) for different mesh sizes. All the identifications started
 426 from the same initial guess; they are conducted on a real test (not on gen-
 427 erated data from known parameters as for the previous study). When the
 428 number of elements increases, the identified parameters converge to their op-
 429 timized value, as the evolution of the error shows. The compromise between
 430 computational time and accuracy was set to around 1200 elements.

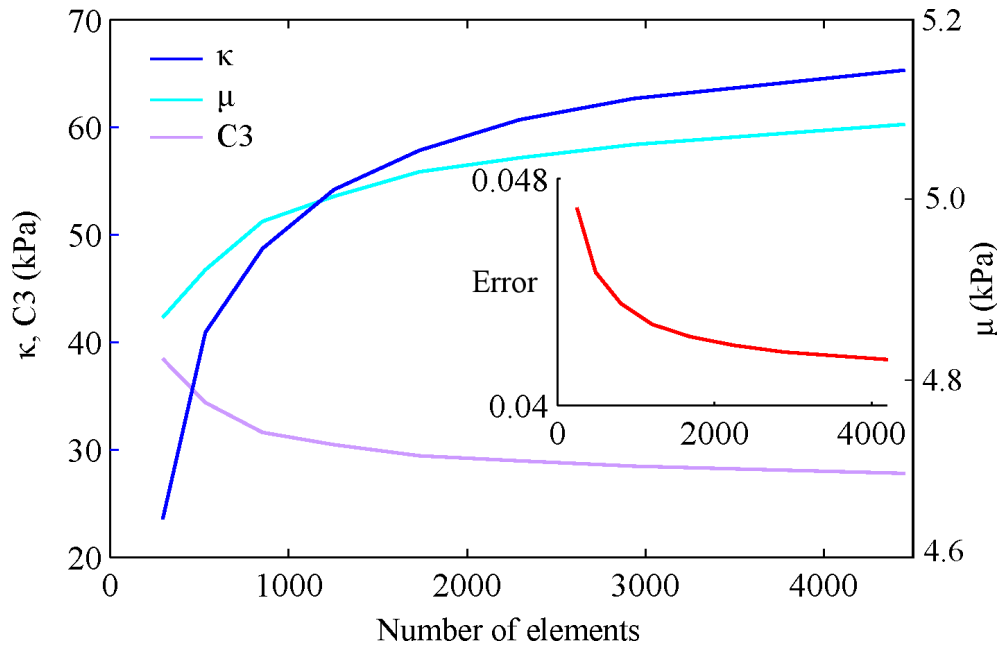


Figure 9: Evolution of the identified parameters for law B (see Tab. 3) with respect to the total number of elements, for one sample of rat G. The evolution of the error e is displayed in red.

431 *Sensitivity analysis.* We evaluated the sensitivity of the error to small vari-
 432 ations of the constitutive parameters. Fig. 10 and 11 display the evolution
 433 of the error for the hyperelastic law given in Eq. (13) with a variation of
 434 $\pm 10\%$ around the identified value of the parameters κ , C_1 and C_3 , and for a
 435 viscoelastic law (potential of Eq. (13) + viscous contribution) with a varia-
 436 tion of $\pm 20\%$ around the identified value of the time parameter τ . In both
 437 cases, when we look at the scales, the error map is rather flat, but it is how-
 438 ever slightly influenced by small variations of the parameters. In particular,
 439 the first order parameter (C_1) has a strong influence, while C_3 and κ are
 440 rather coupled (the error displays a valley). However, we could check that a
 441 minimum exists by testing different initial guesses for all the samples and by
 442 checking that the identification always converges to the same set of paramet-
 443 ers. For the viscoelastic identification, there is a clear minimum of the error
 444 with respect to τ .

445 5.4. Hyperelastic identification

446 For both the hyperelastic and viscoelastic identifications, information on
 447 the thickness is required. The measured thickness for all the tested samples
 448 was $442 \pm 34 \mu\text{m}$, $503 \pm 57 \mu\text{m}$ and $519 \pm 70 \mu\text{m}$ for rats G, I and J respec-
 449 tively. For different reasons (rupture, poor quality of the image registration)
 450 some of these tests could not be fully post-processed.

451 *Volumetric potential.* As mentioned in Sec.3.2, three volumetric potentials
 452 are tested. Fig. 12 displays the error obtained with these three volumet-
 453 ric potentials combined with the same isochoric potential of type B (which
 454 parameters are not identified), for all the samples of a single rat. We can

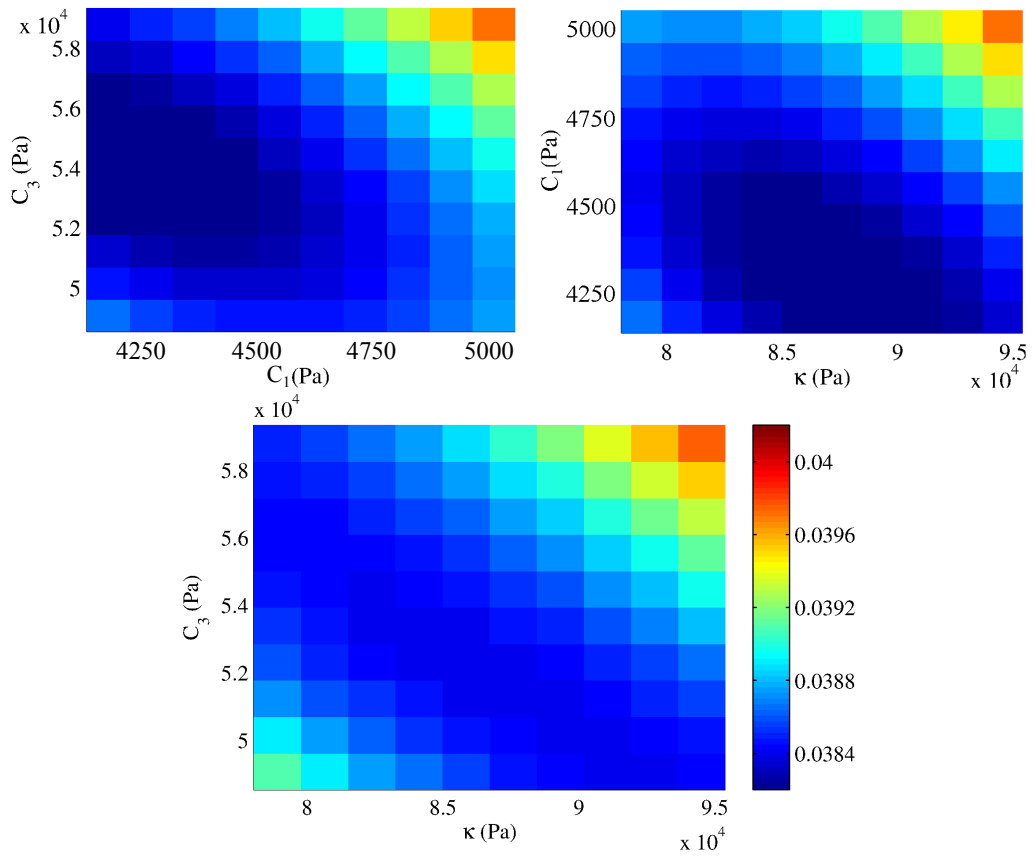


Figure 10: Sensitivity of the error to small variations of the constitutive parameters. The sensitivity study is conducted on a sample of rat I tested at 0.2 Hz, the constitutive law is of type B. For each graph, the respective third parameter is kept constant.

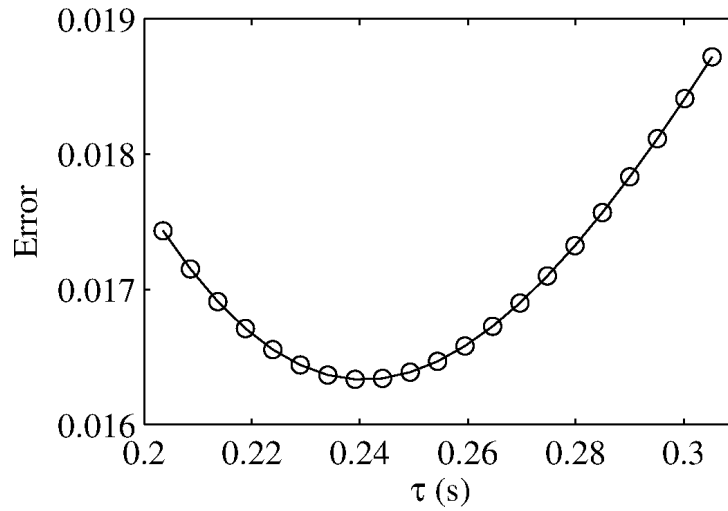


Figure 11: Sensitivity of the error to small variations of parameter τ of a viscoelastic law. The sensitivity study is conducted on a sample of rat I tested at 0.2 Hz, the constitutive law is of type E. Parameters of the elastic contribution are kept constant.

455 see that Sussman-Bathes and Ogden potentials give equal results while the
 456 penalty potential is either equivalent or worse. Therefore, the volumetric
 457 potential used in the following parts will always be the Ogden form.

458 *Identification of volumetric and isochoric parameters.* Fig. 13 shows the
 459 results obtained for each tested frequency among all the tested samples (three
 460 rats). We can see the comparison between the combinations of potentials
 461 given in Tab. 3. This shows that the performances of these forms of potential
 462 give rather similar results, but the exponential form (law P) gives the best
 463 fit for each frequency. A Mann-Whitney statistical test computed on all the
 464 samples shows that law C gives significantly poorer results than laws A, B
 465 and P.

466 Tab. 4 gives the value of the identified parameters for these hyperelastic

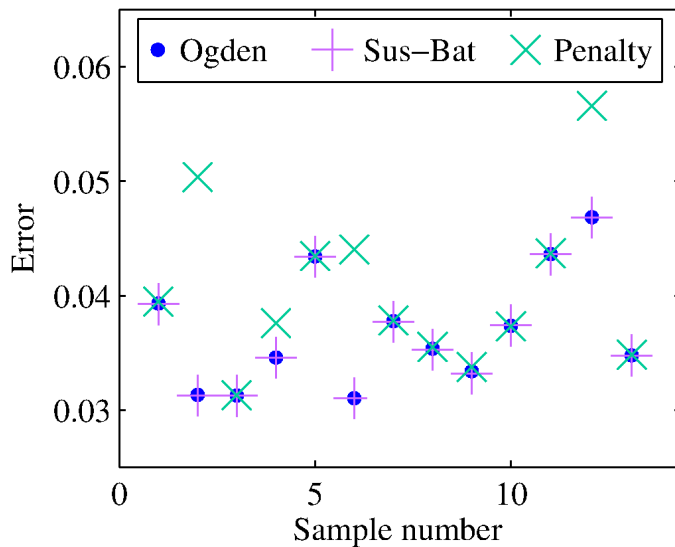


Figure 12: Comparison of the performance of Ogden, Sussman-Bathe and penalty volumetric potentials for parenchyma samples from the same rat. The volumetric potential is always associated to the same isochoric potential of type B (see Tab. 3).

467 potentials. As there is no statistical difference between the identified param-
 468 eters for the varying tested frequencies, the values are averaged over all the
 469 samples and all the frequencies. The identified value of κ is averaged over
 470 all the potentials as this value is independent from the form of the isochoric
 471 potential.

472 5.5. Viscoelastic identification

473 Fig. 14 displays an example of hyper- versus viscohyperelastic identifi-
 474 cation. For force versus displacement curves in the direction of the applied
 475 load, we can see that a hyperelastic potential represents the non-linearity of
 476 the material but only adding a viscous contribution can lead to the correct
 477 hysteresis.

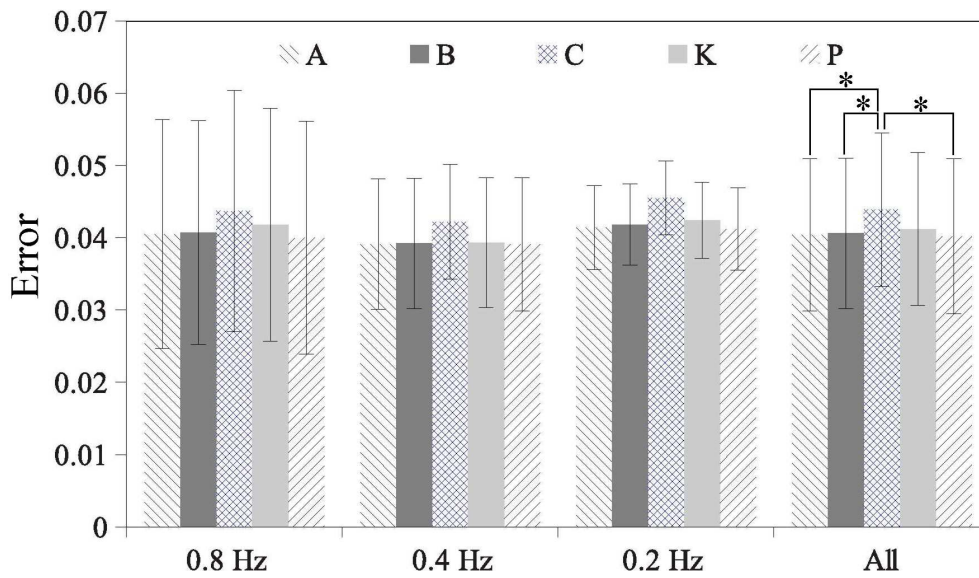


Figure 13: Comparison of the performance of different forms of hyperelastic potentials for various frequencies, among all the tested samples (12 at 0.8 Hz, 12 at 0.4 Hz, 14 at 0.2 Hz, all from three different rats). The average \pm SD of the error is displayed. * corresponds to $p \leq 0.05$.

Law	Parameter	Value	Unit
	κ	$7.25e4 \pm 2.74e4$	Pa
A	C_1	$2.45e3 \pm 8.95e2$	Pa
	C_2	$3.69e3 \pm 1.96e3$	Pa
	C_3	$3.22e4 \pm 1.81e4$	Pa
B	C_1	$2.87e3 \pm 9.05e2$	Pa
	C_3	$3.83e4 \pm 1.63e4$	Pa
K	C_1	$3.43e3 \pm 1.05e3$	Pa
	C_4	$1.34e5 \pm 8.30e4$	Pa
P	k_1	$4.70e3 \pm 1.60e3$	Pa
	k_2	5.90 ± 1.51	-

Table 4: Identified parameters (average \pm SD) for purely elastic potentials.

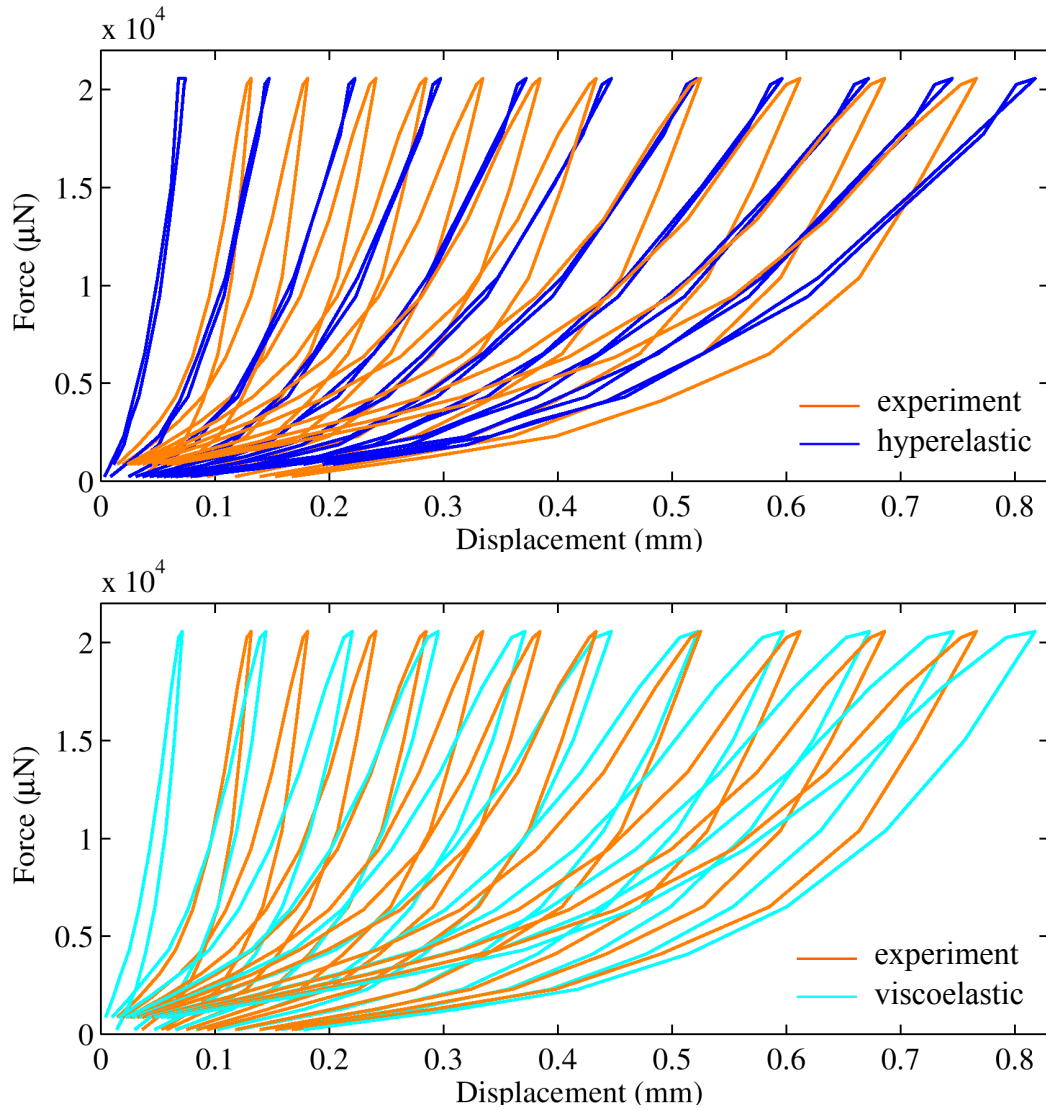


Figure 14: Comparison of the force versus displacement curve along axis x for one sample of rat G and for several nodes: experimental, computed with a hyperelastic constitutive law B ($\kappa = 57.6$ kPa, $C_1 = 1.36$ kPa and $C_3 = 71.9$ kPa) and with a visco-hyperelastic law E ($\kappa = 62.4$ kPa, $C_1 = 2.78$ kPa, $C_3 = 41.8$ kPa, $\tau = 0.293$). The hyperelastic curve has been smoothed not to represent some artifacts created by vibrations. The experimental displacement is computed by image registration.

478 Fig. 15 displays all the results obtained by identification of the param-
 479 eters of the hyperelastic potentials and of the corresponding viscoelastic
 480 laws. We can see the significant increase in accuracy obtained with the
 481 viscoelastic laws, especially when the frequency decreases. Mann-Whitney
 482 post-processing of the error values reveals that adding a viscous contribution
 483 significantly increases the quality of the identification; the p-value is below
 484 0.0001 for all couples of laws (A, B, C, K, L *vs.* D, E, F, L, M respectively).

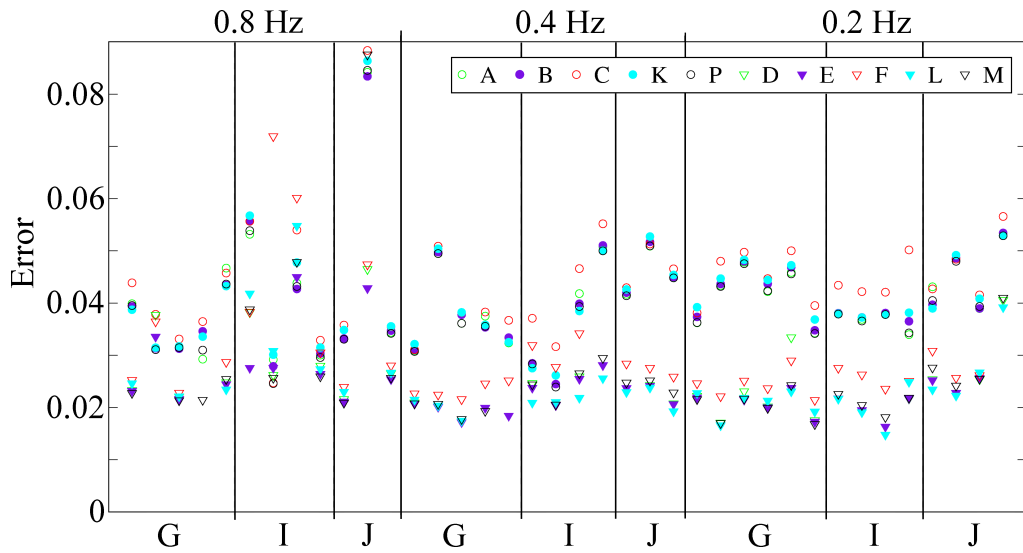


Figure 15: Distribution of the error obtained for all the samples for the identified hyperelastic potentials, with and without a viscous contribution. Laws D, E, F, L and M (triangles) are viscoelastic laws that correspond to the hyperelastic potentials A, B, C, K, P (circles) modified with a viscous contribution. X-axis: G, I, J are the three tested rats. Top: tested frequencies.

485 Fig. 16 displays the identification results for the viscoelastic laws for the
 486 tested frequencies. Altogether, the performance of law F is significantly lower
 487 than all the other laws (the p-factor is ≤ 0.05 with respect to law D, ≤ 0.001

488 with respect to law M and ≤ 0.0001 with respect to laws E and L) . Tab.
 489 5 displays the identified values for the parameters of the viscoelastic laws.
 490 The parameters related to the elastic potentials (C_i, κ, k_i) are averaged over
 491 all the samples and all the frequencies as the influence of the frequency is
 492 negligible. The obtained values are actually similar to those obtained with
 493 the purely elastic identification (Tab. 4) which makes sense as the latter
 494 values are the initial guess of the viscoelastic identification. However, τ
 495 significantly increases when the frequency decreases ($p \leq 0.0001$); its values
 496 are therefore given per frequency.

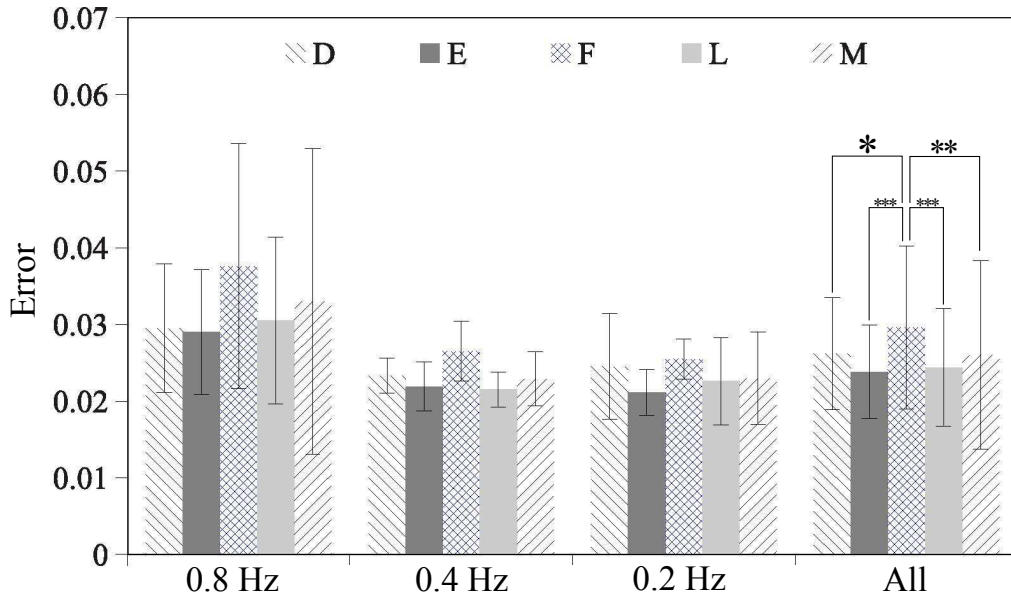


Figure 16: Comparison of the performance of different forms of viscoelastic potentials for various frequencies, among all the tested samples (12 at 0.8 Hz, 12 at 0.4 Hz, 14 at 0.2 Hz, all from three different rats). * corresponds to $p \leq 0.05$, ** corresponds to $p \leq 0.001$, *** corresponds to $p \leq 0.0001$.

Law	Parameter	Value	Unit
	κ	$7.06e4 \pm 2.93e4$	Pa
D	C_1	$3.22e3 \pm 9.53e2$	Pa
	C_2	$2.04e3 \pm 2.86e3$	Pa
	C_3	$2.92e4 \pm 1.52e4$	Pa
E	C_1	$3.54e3 \pm 9.48e2$	Pa
	C_3	$3.30e4 \pm 1.58e4$	Pa
L	C_1	$4.04e3 \pm 1.07e3$	Pa
	C_4	$9.62e4 \pm 5.09e4$	Pa
M	k_1	$5.58e3 \pm 1.69e3$	Pa
	k_2	4.86 ± 1.42	-

Frequency	Parameter	Value	Unit
0.8 Hz	τ	$5.06e-2 \pm 2.53e-2$	s
0.4 Hz		$1.23e-1 \pm 3.87e-2$	
0.2 Hz		$2.57e-1 \pm 4.22e-2$	

Table 5: Identified parameters for viscoelastic potentials.

497 **6. Discussion**

498 This paper presents a method to determine material parameters for the
499 lung parenchyma using advanced methods from both the experimental and
500 the theoretical point of view. Thanks to this method, we obtain a reliable
501 viscoelastic constitutive law that is suitable for Finite Element calculations.

502 The experimental protocol has been improved since (Rausch et al., 2011).
503 Measuring the thickness of each sample individually revealed its non-negligible
504 variability throughout the set of samples; this distribution is now taken into
505 account in the simulation. The other main improvement is the use of an op-
506 tical method to determine the displacement field at the sample surface. It is
507 worth noticing that as the samples are really thin, we can consider that this
508 surface information is sufficient to describe the behavior of the tissue. In our
509 case, knowing the displacement field is of high importance as we are partic-
510 ularly interested in the lateral contraction of the sample. When we optically
511 check the results of the image registration by superimposing the image and
512 the corresponding mesh (Fig. 8 for instance), we can see that this optical
513 method applied to the natural pattern of the parenchyma gives fully satis-
514 factory results, despite some light reflections at the sample surface. These
515 artifacts are indeed smoothed by the Finite-Element kinematics inherent to
516 the image registration method.

517 The theoretical constitutive framework used in this paper is adapted from
518 an existing model proposed in (Holzapfel and Gasser, 2001). It allows the
519 description of the non-linear elasticity as well as the viscosity for both the
520 isochoric and the volumetric components of the deformation, not only the
521 isochoric one.

522 In the present work, a quantitative determination of elastic as well as vis-
523 cous properties of rat lung parenchyma is provided. The order of magnitude
524 of the strain in our protocol is 0 to 45 %. In this range, the non-linear elas-
525 tic behaviour of lung parenchyma is equally well described by a polynomial
526 potential of degree ≥ 3 associated to a linear component (degree 1) or an
527 exponential potential. No significant influence of the testing frequency was
528 found in the identified elastic parameters. For the volumetric aspect of the
529 law, we could determine that both Ogden and Sussman-Bathe give the same
530 result and that the volumetric parameter κ is rather accurately identified (c.f.
531 low standard deviation). In (Rausch et al., 2011), values for the parameters
532 for a law of type B are given. C_1 is similar to the one of this paper, while
533 κ and C_3 are smaller. The explanation can come from a better description
534 of the lateral contraction in the present paper, that highly influences the
535 determination of κ , as well as the consideration of the actual thickness of the
536 sample.

537 Adding a viscous component to the identified non-linear elastic constitu-
538 tive law significantly increases the quality of the identification, especially at
539 low frequency where the error is cut by half compared to the purely elas-
540 tic case. It allows the description of the experimentally observed hysteresis
541 loop. The elastic contribution of the law is rather insensitive to the frequency,
542 but the time constant τ significantly decreases with increasing frequency. It
543 shows that the lower the frequency, the higher the viscous effects.

544 The main limitation of this work is that the uniaxial tension loading
545 mode does not correspond to the mainly volumetric deformations the tissue
546 would be subjected to in reality. It is not guaranteed that the constitutive

547 law determined in this paper for an isochoric-dominated loading would not
548 be influenced by a volumetric-dominated loading. Identifying the volumetric
549 contribution using the width evolution is however a first step towards an
550 accurate estimation of the compressible behavior of the homogeneous lung
551 parenchyma.

552 A possible improvement for the presented method would be to replace
553 the two optimization processes (image registration and inverse analysis) by
554 a single one. It would consist in improving the mechanical regularization in
555 the image registration, currently purely elastic, by taking into account the
556 actual material law that is to be identified. This type of mechanical/optical
557 identification method is described for instance in (Réthoré, 2010) and could
558 be implemented in our in-house code in a straightforward way.

559 The present experimental protocol and identification method are now to
560 be applied for more biological tissues. Although they are particularly adapted
561 to compressible material, they could also be used for any soft biological tissue,
562 possibly requiring the addition of a random pattern on the surface of the
563 sample. Future work is to investigate the viscoelastic properties of human
564 lung parenchyma as well as parenchyma samples altered with ARDS. These
565 data could then be included into the computational model of the respiratory
566 system that is developed in our group.

567 **Acknowledgement 1.** *Support by the German Science Foundation/Deutsche*
568 *Forschungsgemeinschaft DFG (Wa 1521/9 and Uh 88/7) is gratefully ac-*
569 *knowledged.*

570 **Appendix A. Computation of the elastic stress and elasticity ten-**
571 **sors**

572 *Appendix A.1. Kinematic quantities*

573 The decoupled form of the potential requires expressing modified strain
574 tensors. We define \mathbf{F} as the deformation gradient and $J = \det \mathbf{F}$ is the vol-
575 ume change. The Cauchy-Green strain tensor is therefore $\mathbf{C} = \mathbf{F}^T \mathbf{F}$. In the
576 case of a decoupled hyperelastic potential, we apply a volumetric/isochoric
577 multiplicative split of the deformation.

$$\mathbf{F} = J^{1/3} \bar{\mathbf{F}} \quad (\text{A.1})$$

$$\mathbf{C} = J^{2/3} \bar{\mathbf{C}} \quad (\text{A.2})$$

578 where $\bar{\mathbf{F}}$ and $\bar{\mathbf{C}}$ are the modified deformation gradient and Green-Lagrange
579 tensor respectively, representing the isochoric part of the deformation. The
580 strain invariants are defined as:

$$\begin{cases} I_1(\mathbf{C}) = \text{tr } \mathbf{C} \\ I_2(\mathbf{C}) = \frac{1}{2} ((\text{tr } \mathbf{C})^2 - \text{tr } \mathbf{C}^2) \\ I_3(\mathbf{C}) = \det \mathbf{C} \end{cases} \quad (\text{A.3})$$

581 The modified invariants associated with the isochoric contribution are
582 defined as :

$$\bar{I}_i = J^{-2/3} I_i \text{ for } i = 1, 3 \Rightarrow \bar{I}_3 = 1 \quad (\text{A.4})$$

$$\bar{I}_2 = J^{-4/3} I_2 \quad (\text{A.5})$$

583 *Appendix A.2. Hyperelastic potentials*

584 Decoupling an isotropic hyperelastic potential leads to the following form:

$$\psi(\mathbf{C}) = \psi_{vol}(J) + \psi_{iso}(\bar{I}_1, \bar{I}_2) \quad (\text{A.6})$$

585 Adding a viscous contribution to both the isochoric and the volumetric
586 part of the hyperelastic potential corresponds to:

$$\psi(\mathbf{C}, \mathbf{\Gamma}_{vol}, \bar{\mathbf{\Gamma}}) = \psi_{vol}(J, \mathbf{\Gamma}_{vol}) + \psi_{iso}(\bar{I}_1, \bar{I}_2, \bar{\mathbf{\Gamma}}) \quad (\text{A.7})$$

587 where $\mathbf{\Gamma}_{vol}$ and $\bar{\mathbf{\Gamma}}$ are kinematic internal variables that characterize the
588 non-equilibrium state of the deformation process. It can be further split the
589 following way:

$$\psi(\mathbf{C}, \mathbf{\Gamma}_{vol}, \bar{\mathbf{\Gamma}}) = \psi_{vol}^\infty(J) + \gamma_{vol}(\mathbf{\Gamma}_{vol}) + \psi_{iso}^\infty(\bar{I}_1, \bar{I}_2) + \gamma_{iso}(\bar{\mathbf{\Gamma}}) \quad (\text{A.8})$$

For the next section, we define the following quantities:

$$\psi_i = \frac{\partial \psi_{iso}^\infty}{\partial \bar{I}_i}, \quad i = 1, 2 \quad (\text{A.9})$$

$$p = \frac{\partial \psi_{vol}^\infty}{\partial J} \quad (\text{A.10})$$

$$\psi_{ij} = \frac{\partial^2 \psi_{iso}^\infty}{\partial \bar{I}_i \partial \bar{I}_j}, \quad i, j = 1, 2 \quad (\text{A.11})$$

590 *Appendix A.3. Stress tensors*

591 According to the work of (Holzapfel and Gasser, 2001), the elastic second
592 Piola-Kirchhoff stress tensors are defined by:

$$\mathbf{S}_{vol}^\infty = J p \mathbf{C}^{-1} \quad (\text{A.12})$$

$$\mathbf{S}_{iso}^\infty = J^{-2/3} \mathbb{P} : [2\psi_1 \mathbf{I} + 2\psi_2 (\bar{I}_1 \mathbf{I} - \bar{\mathbf{C}})] \quad (\text{A.13})$$

593 where $\mathbb{P} = \mathbb{I} - \frac{1}{3} \mathbf{C}^{-1} \otimes \mathbf{C}$ is a fourth-order projector. As mentioned before,
 594 the fictitious stress tensors \mathbf{Q}_{vol} and \mathbf{Q}_{iso} associated with these elastic stress
 595 tensors follow an evolution equation given by Eq. (7).

596 *Appendix A.4. Elasticity tensors*

597 According to the work of (Holzapfel and Gasser, 2001), the elastic con-
 598 tribution of the elasticity tensors are defined by:

$$\mathbb{C}_{vol}^\infty = J \tilde{p} \mathbf{C}^{-1} \otimes \mathbf{C}^{-1} - 2Jp \mathbf{C}^{-1} \odot \mathbf{C}^{-1} \quad (\text{A.14})$$

599

$$\mathbb{C}_{iso}^\infty = \sum_{i=1,2} \mathbb{C}_{iso,i}^\infty \quad (\text{A.15})$$

where:

$$\tilde{p} = p + J \frac{\partial p}{\partial J} \quad (\text{A.16})$$

$$\begin{aligned} \mathbb{C}_{iso,i}^\infty = \mathbb{P} : \hat{\mathbb{C}}_i^\infty : \mathbb{P}^T + \frac{2}{3} \left(J^{2/3} \hat{\mathbf{S}}_i^\infty : \mathbf{C} \right) \tilde{\mathbb{P}} \\ - \frac{2}{3} \left(\mathbf{C}^{-1} \otimes \mathbf{S}_{iso,i}^\infty + \mathbf{S}_{iso,i}^\infty \otimes \mathbf{C}^{-1} \right) \end{aligned} \quad (\text{A.17})$$

600

$$\hat{\mathbb{C}}_i^\infty = 4J^{-4/3} \sum_{j=1,2} (\psi_{ij} \mathbf{D}_i \otimes \mathbf{D}_j + \psi_i \mathbb{D}_i) \quad (\text{A.18})$$

601

$$\mathbf{D}_i = \frac{\partial \bar{I}_i}{\partial \bar{C}}, \quad \mathbb{D}_i = \frac{\partial \mathbf{D}_i}{\partial \bar{C}} \quad (\text{A.19})$$

602

$$\hat{\mathbf{S}}_i^\infty = 2\psi_i \mathbf{D}_i, \quad \mathbf{S}_{iso,i}^\infty = J^{-2/3} \mathbb{P} : \hat{\mathbf{S}}_i^\infty \quad (\text{A.20})$$

603

$$\tilde{\mathbb{P}} = \mathbf{C}^{-1} \odot \mathbf{C}^{-1} - \frac{1}{3} \mathbf{C}^{-1} \otimes \mathbf{C}^{-1} \quad (\text{A.21})$$

604 The viscous contribution can be calculated from the elastic contribution,
605 see Appendix B.

606 **Appendix B. Computation of the viscous stress and elasticity ten-**
607 **sors**

608 *Appendix B.1. Fictitious stress tensor*

609 To solve the differential equation (7), we apply the following method:

$$\dot{\mathbf{Q}} + \frac{1}{\tau} \mathbf{Q} = \beta \dot{\mathbf{S}} \quad (\text{B.1})$$

$$\Leftrightarrow \dot{\mathbf{Q}} - \beta \dot{\mathbf{S}} = -\frac{1}{\tau} \mathbf{Q} \quad (\text{B.2})$$

$$(\text{B.3})$$

610 Once the elastic stress tensor \mathbf{S} is computed at time step $n + 1$, we use
611 a Newton scheme to compute the fictitious stress tensor at step $n + 1$, using
612 the history of these tensors:

$$\begin{aligned} (\mathbf{Q} - \beta \mathbf{S})_{n+1} &= (\mathbf{Q} - \beta \mathbf{S})_n \\ &+ (1 - \theta) \Delta t \underbrace{\left(\dot{\mathbf{Q}} - \beta \dot{\mathbf{S}} \right)_n}_{-\frac{1}{\tau} \mathbf{Q}_n} + \theta \Delta t \underbrace{\left(\dot{\mathbf{Q}} - \beta \dot{\mathbf{S}} \right)_{n+1}}_{-\frac{1}{\tau} \mathbf{Q}_{n+1}} \end{aligned} \quad (\text{B.4})$$

$$\Leftrightarrow \mathbf{Q}_{n+1} = \lambda_1 [\lambda_2 \mathbf{Q}_n + \beta (\mathbf{S}_{n+1} - \mathbf{S}_n)] \quad (\text{B.5})$$

613 with

$$\lambda_1 = \frac{\tau}{\tau + \theta\Delta t}, \quad \lambda_2 = 1 - \frac{(1 - \theta)\Delta t}{\tau} \quad (\text{B.6})$$

614 *Appendix B.2. Viscous elasticity tensor*

615 As described in (Holzapfel and Gasser, 2001), the overall elasticity tensor
616 at time step $n + 1$ is calculated as the sum of the elastic tensor and the
617 viscous tensor, which leads to:

$$\mathbb{C}_{n+1} = (1 + \delta) \left[\mathbb{C}_{vol}^\infty + \sum_{i=1,2} \mathbb{C}_{iso,i}^\infty \right]_{n+1} \quad (\text{B.7})$$

618 where $\delta = \beta \exp(-\Delta t/2\tau)$ as we consider the viscous constants τ and β
619 to be the same for isochoric and volumetric contributions.

620 Balzani, D., Neff, P., Schröder, J., Holzapfel, G., 2006. A polyconvex frame-
621 work for soft biological tissues. adjustment to experimental data. Interna-
622 tional Journal of Solids and Structures 43, 6052–6070.

623 Delfino, A., Stergiopoulos, N., Moore, J.E., Meister, J.J., 1997. Residual strain
624 effects on the stress field in a thick wall finite element model of the human
625 carotid bifurcation. Journal of Biomechanics 30, 777–786.

626 Dolhnikoff, M., Mauad, T., Ludwig, M.S., 1999. Extracellular matrix and
627 oscillatory mechanics of rat lung parenchyma in bleomycin-induced fibrosis.
628 American Journal of Respiratory and Critical Care Medicine 160, 1750–
629 1757.

- 630 Doll, S., Schweizerhof, K., 2000. On the development of volumetric strain
631 energy functions. *Journal of applied mechanics* 67, 17–21.
- 632 Fischer, B., Modersitzki, J., 2008. Ill-posed medicine - an introduction to
633 image registration. *Inverse Problems* 24, 034008.
- 634 Fung, Y., 1993. *Biomechanics: Mechanical Properties of Living Tissues*.
635 Springer.
- 636 Gao, J., Huang, W., Yen, R.T., 2006. Mechanical properties of human lung
637 parenchyma. *Biomedical Sciences Instrumentation* 42, 172–180.
- 638 Haber, E., Heldmann, S., Modersitzki, J., 2009. A framework for image-
639 based constrained registration with an application to local rigidity. *Linear*
640 *Algebra and its Applications* 431, 459–470.
- 641 Haber, E., Modersitzki, J., 2006. A multilevel method for image registration.
642 *SIAM Journal on Scientific Computing* 27, 1594–1607.
- 643 Holzapfel, G., Gasser, T., 2001. A viscoelastic model for fiber-reinforced
644 composites at finite strains: Continuum basis, computational aspects and
645 applications. *Computer methods in Applied Mechanics and Engineering*
646 190, 4379–4403.
- 647 Ingenito, E., Mark, L., Davison, B., 1994. Effects of acute lung injury on
648 dynamic tissue properties. *Journal of Applied Physiology* 77, 2689–2697.
- 649 Kallet, R.H., Katz, J.A., 2003. Respiratory system mechanics in acute res-
650 piratory distress syndrome. *Respiratory care clinics of North America* 9,
651 297–319.

- 652 Lester, H., Arridge, S.R., 1999. A survey of hierarchical non-linear medical
653 image registration. *Pattern recognition* 32, 129–149.
- 654 Mann, H., Whitney, D., 1947. On a test of whether one of two random vari-
655 ables is stochastically larger than the other. *The annals of mathematical*
656 *statistics* 18, 50–60.
- 657 Martin, C., Uhlig, S., Ullrich, V., 1996. Videomicroscopy of methacholine-
658 induced contraction of individual airways in precision-cut lung slices. *Eu-*
659 *ropean Respiratory Journal* 9, 2479–2487.
- 660 Mijailovich, S.M., Stamenovic, D., Brown, R., Leith, D.E., Fredberg, J.J.,
661 1994. Dynamic moduli of rabbit lung tissue and pigeon ligamentum
662 propatagiale undergoing uniaxial cyclic loading. *Journal of Applied Phys-*
663 *iology* 76, 773–782.
- 664 Modersitzki, J., 2004. *Numerical Methods for Image Registration (Numerical*
665 *Mathematics and Scientific Computation)*. Oxford university press.
- 666 Navajas, D., Maksym, G.N., Bates, J.H., 1995. Dynamic viscoelastic non-
667 linearity of lung parenchymal tissue. *Journal of Applied Physiology* 79,
668 348–356.
- 669 Ogden, R., 1974. On the overall moduli of non-linear elastic composite ma-
670 terials. *Journal of the Mechanics and Physics of Solids* 22, 541–553.
- 671 Pinart, M., Faffe, D., Sapiña, M., Romero, P., 2011. Dynamic nonlinearity of
672 lung tissue: effects of strain amplitude and stress level. *Journal of Applied*
673 *Physiology* 110, 653–660.

- 674 Rausch, S., Martin, C., Bornemann, P., Uhlig, S., Wall, W., 2011. Material
675 model of lung parenchyma based on living precision-cut lung slice testing.
676 *Journal of the Mechanical Behavior of Biomedical Materials* 4, 583–592.
- 677 Rocco, P.R., Negri, E.M., Kurtz, P.M., Vasconcellos, F.P., Silva, G.H.,
678 Capelozzi, V.L., Romero, P.V., Zin, W.A., 2001. Lung tissue mechan-
679 ics and extracellular matrix remodeling in acute lung injury. *American*
680 *Journal of Respiratory and Critical Care Medicine* 164, 1067–1071.
- 681 Romero, P.V., Faffe, D.S., Cañete, C., 2011. Dynamic nonlinearity of lung
682 tissue: frequency dependence and harmonic distortion. *Journal of Applied*
683 *Physiology* 111, 420–426.
- 684 Réthoré, J., 2010. A fully integrated noise robust strategy for the identifi-
685 cation of constitutive laws from digital images. *International Journal for*
686 *Numerical Methods in Engineering* 84 (6), 631–660.
- 687 Suki, B., Bates, J., 2011. Lung tissue mechanics as an emergent phenomenon.
688 *Journal of Applied Physiology* 110, 1111–1118.
- 689 Wall, W.A., Wiechert, L., Comerford, A., Rausch, S., 2010. Towards a com-
690 prehensive computational model for the respiratory system. *International*
691 *Journal for Numerical Methods in Biomedical Engineering* 26, 807–827.
- 692 Yeoh, O., 1993. Some forms of the strain energy function for rubber. *Rubber*
693 *Chemistry and Technology* 66, 754–771.
- 694 Yuan, H., Ingenito, E., Suki, B., 1997. Dynamic properties of lung
695 parenchyma: mechanical contributions of fiber network and interstitial
696 cells. *Journal of Applied Physiology* 83, 1420–31, discussion 1418–9.